NANO · MICRO small
www.small-journal.com

Unlocking Deep and Fast Potassium-Ion Storage through Phosphorus Heterostructure

Xiaoju Zhao, Shitao Geng, Tong Zhou, Yan Wang, Shanshan Tang, Zongtao Qu, Shuo Wang, Xiao Zhang, Qiuchen Xu, Bin Yuan, Zhaofeng Ouyang, Huisheng Peng, Shaochun Tang, and Hao Sun**

Potassium-ion battery represents a promising alternative of conventional lithium-ion batteries in sustainable and grid-scale energy storage. Among various anode materials, elemental phosphorus (P) has been actively pursued owing to the ideal natural abundance, theoretical capacity, and electrode potential. However, the sluggish redox kinetics of elemental P has hindered fast and deep potassiation process toward the formation of final potassiation product (K_3P), which leads to inferior reversible capacity and rate performance. Here, it is shown that rational design on black/red P heterostructure can significantly improve K-ion adsorption, injection and immigration, thus for the first time unlocking K_3P as the reversible potassiation product for elemental P anodes. Density functional theory calculations reveal the fast adsorption and diffusion kinetics of K-ion at the heterostructure interface, which delivers a highly reversible specific capacity of 923 mAh g^{-1} at 0.05 A g^{-1}, excellent rate capability (335 mAh g^{-1} at 1 A g^{-1}), and cycling performance (83.3% capacity retention at 0.8 A g^{-1} after 300 cycles). These results can unlock other sluggish and irreversible battery chemistries toward sustainable and high-performing energy storage.

1. Introduction

Potassium-ion batteries (PIBs) are promising candidates for sustainable and grid-scale energy storage.[1] With a much higher abundance in the Earth's crust (1.5 wt% of potassium vs 16 ppm of lithium),[2] potassium (K) is an appealing alternative to alleviate the sustainability concerns of lithium-ion batteries, thus attracting widespread interests from both academic and industrial communities. Among various PIB anodes, elemental phosphorus, especially red phosphorus (RP) presents a desirable candidate owing to its low cost, high theoretical specific capacity (2596 mAh g^{-1} for K_3P) and ideal redox potential (≈0.6 V versus K/K^+). However, the sluggish reaction kinetics of large-radius K-ion generally leads to poor battery rate capabilities. In addition, the poor electrical conductivity (≈10^{-14} S cm^{-1}) of RP hinders the efficient electron transfer which further sacrifices the rate capability.[2,3] These lead to the adsorption of K ions on the surface of RP, which resulted in dendrite formation at higher current densities.[4–8] Therefore, the pursuit of deep potassiation product (e.g., K_3P) remains a grand challenge of the whole field, particularly under high-rate conditions. Considerable efforts have been devoted to resolving the above challenges, such as size/morphologic optimization and carbon incorporation,[9,10] which shows improved electron and ion transfer to some extent. However, the root of the problem, that is, the intrinsically sluggish diffusion and reaction kinetics of elemental P has not been fully tackled. Therefore, realizing deep and reversible K-ion storage based on elemental P anode is crucial but remains challenging to date,[11–13] which hinders the practical PIBs.

X. Zhao, S. Geng, Y. Wang, S. Tang, Z. Qu, S. Wang, X. Zhang, Q. Xu, B. Yuan, Z. Ouyang, H. Sun
Frontiers Science Center for Transformative Molecules
School of Chemistry and Chemical Engineering
and Zhangjiang Institute for Advanced Study
Shanghai Jiao Tong University
Shanghai 200240, China
E-mail: haosun@sjtu.edu.cn

T. Zhou
School of Physics and Optoelectronic Engineering
Shandong University of Technology
Zibo 255049, China

The ORCID identification number(s) for the author(s) of this article can be found under https://doi.org/10.1002/smll.202301750.

DOI: 10.1002/smll.202301750

H. Peng
State Key Laboratory of Molecular Engineering of Polymers
Department of Macromolecular Science
and Laboratory of Advanced Materials
Fudan University
Shanghai 200438, China

S. Tang
Key National Laboratory of Solid State Microstructures
Department of Materials Science and Engineering
Collaborative Innovation Center of Advanced Microstructures
Jiangsu Key Laboratory of Artificial Functional Materials
College of Engineering and Applied Sciences
Nanjing University
Nanjing 210093, China
E-mail: tangsc@nju.edu.cn

Here we show that rational heterostructure engineering can be an effective strategy to facilitate the sluggish K-ion diffusion and reaction kinetics in elemental P anode. We design and prepare altered black phosphorus/red phosphorus heterostructure on multi-walled carbon nanotubes (BRPH@MWCNT) via a facile and scalable approach. Abundant heterostructure interfaces significantly promote the K-ion adsorption, injection and immigration, delivering a remarkable specific capacity of 923 mAh g^{-1} at 0.05 A g^{-1} and excellent rate capability of 335 mAh g^{-1} at 1 A g^{-1}, setting new records for elemental P-based anodes of PIBs.[14] Decent cycling stability during 300 cycles is demonstrated at 0.8 A g^{-1} originated from the KF-rich interfacial layer induced by P heterostructure, which effectively improves the electrochemical reversibility. *Operando* X-ray diffraction and time-of-flight secondary ion mass spectroscopy confirm the formation of K_3P as the deep potassiation product, which represents a breakthrough for elemental P anodes toward deep potassiation electrochemistry. Our results can unlock the long-standing bottlenecks of elemental P anode for PIBs, and open a new avenue for reviving other sluggish and irreversible battery chemistries.

2. Results and Discussion

We synthesized the BRPH@MWCNT through a solvent-thermal method (see details in Experimental Section).[15] Briefly, ethane diamine served as a phosphorous chain attacker and structure reconstruction agent, which induced the phase transition from RP to BP under hydrothermal condition. Each BP/RP grain was comprised of large quantities of BP/RP heterojunctions that created vast heterostructure interfaces, which contributed to K-ion immigration and charge rearrangement (**Figure 1**a). The BP/RP grains were uniformly grown along the axial direction of MWCNT, as verified by scanning electron microscopy (SEM) and energy-dispersive X-ray spectroscopy (EDS) (Figure 1b,c). High-resolution transmission electron microscopy (HRTEM) confirmed the formation of abundant interfaces between BP and RP, which contributed vast heterojunctions to the obtained BRPH@MWCNT (Figure 1d). The abundant heterojunctions are of significant importance for facilitated K-ion immigration compared with previous BP/RP hybrids without rational regulation on the morphology and configuration of heterostructure,[16,17] thus unlocking deep potassiation for PIBs. RP@MWCNT was prepared using the same method without the phase-transformation treatment. The mass ratio between P and MWCNT reactants, solvent, and washing condition was strictly controlled for preparation of RP@MWCNT and BRPH@MWCNT. The P content could be thus controlled for RP@MWCNT and BRPH@MWCNT that guaranteed the effectiveness of the comparison between RP@MWCNT and BRPH@MWCNT (Figures S1 and S2, Supporting Information).[18]

X-ray diffraction (XRD) was performed to verify the formation of BP/RP heterostructure. The broad peaks at 15.2°, 32.4°, and 55.8° indicated the amorphous structure of RP (Figure 1e).[15] For BP/RP heterostructure, the new peaks at 16.4° (5.2 Å), 25.9° (3.4 Å), and 33.0° (2.7 Å) corresponded to the (002), (012), and (004) planes of BP (JCPDS #09–0020) (Figure 1e). Raman spectra (Figure 1f) confirmed the coexistence of BP (A_g^1, B_{2g}, and A_g^2 peaks at 362.8, 444.7, and 470.0 cm^{-1}) and RP (B_1, A_1, and E_1 peaks at 350.1, 395.0, and 450.2 cm^{-1}).[15,19] High-resolution X-ray photoelectron spectroscopy (XPS) showed featured P 2p peaks at 129.8 and 130.6 eV, respectively (Figure S3, Supporting Information). The presence of BP/RP heterostructure resulted in a ≈0.3 eV shift of the P–P splitting peaks, originated from the enhanced interaction between BP and RP as heterostructure formed.[20] The P content in our heterostructure-based hybrid was estimated as ≈73.8 wt% by thermogravimetric analysis (TGA, Figure S4a, Supporting Information), a prerequisite for pursuit of high specific capacities (Table S1, Supporting Information).[2,9,10,21–24] The BP/RP ratio was measured as 0.9 in our BRPH@MWCNT based on the deconvoluted peaks in thermogravimetric curves (Figure S4b, Supporting Information). The BP/RP ratios can be manipulated by varying solvothermal conditions and substantially influence the battery performances (Figure S4 and S5, Supporting Information).

RP, BP, and BP/RP heterostructure show different molecular structures that vary their physicochemical properties (Figure S6, Supporting Information). The RP chain exhibited a "zigzag ladder" structure,[25] and the BP lattice presented a "puckered sheet" structure.[26] The total density of states (DOS) showed different band gaps of 1.14 and 0.46 eV for RP and BP, respectively, suggesting possible spatial charge flows over the heterostructure interface (Figure 1g). The charge rearrangement at the BP/RP heterostructure using differential charge density calculation suggested the substantial electron delocalization at the interface. The built-in electric field was generated and pointed from the electron-deficient BP to the electron-rich RP at the BP/RP interface (Figure 1h).[27] The K-ion transfer can be preferentially driven by the built-in electric field at the heterointerface, which facilitates the immigration of K ions. As showed in Figure S7c, Supporting Information, most of the heterointerfaces formed between BP and RP were vertical to MWCNTs, which could afford sufficient K-ion immigration along the perpendicular direction of MWCNT that facilitated the potassiation process (Figure S7, Supporting Information).[28] The promoted electron transport was originated from BP with high electrical conductivities. In addition, the alignment of BP along the axial direction of MWCNT further promoted the electron transport inside the BRPH@MWCNT (Figure 1d). These together contributed to effective promotion in ion and electron transport for BRPH@MWCNT.

We investigated the potassium-ion storage performance of BRPH@MWCNT, based on an electrolyte comprised of 4 M potassium bis(fluorosulfonyl) imide (KFSI) and 1 M potassium bis(trifluorosulfonyl) imide (KTFSI) in the mixture of ethylene carbonate (EC) and dimethyl carbonate (DMC) with a volume ratio of 1:1. Cyclic voltammetry (CV) showed a prominent wide peak at ≈0.76 V in the initial cathodic sweep (**Figure 2**a), corresponding to the irreversible electrolyte decomposition and solid-electrolyte interphase (SEI) formation.[2,29] The sharp peak at 0.01 V, which shifted to 0.23 V in the subsequent cycles, was associated with the formation of K_xP alloy. The oxidic peaks at 0.78 and 2.36 V could be assigned to the stepwise dealloying of K_xP. The well-overlapped curves in the subsequent cycles implied a good electrochemical reversibility during cycling. The K metal/BRPH@MWCNT half cell delivered a high specific

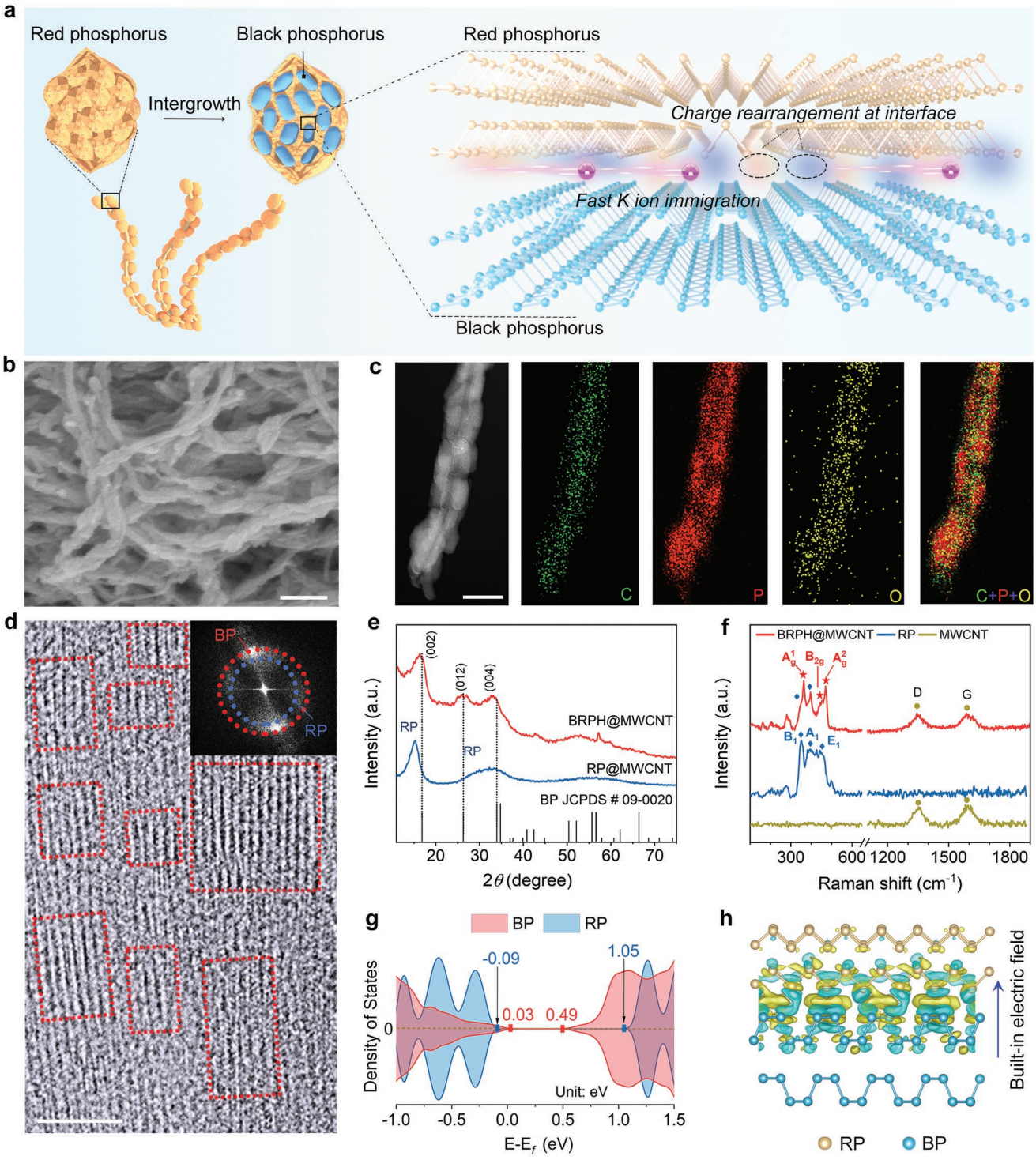

Figure 1. Altered black/red phosphorus heterostructure. a) Schematic illustration of the structure and charge transfer mechanism of BRPH@MWCNT. The BRPH shows a "wheatear" shape and disperses evenly on MWCNT stems. The heterostructure demonstrates promoted K-ion immigration and charge rearrangement with enhanced K-ion storage properties. b) SEM image of BRPH@MWCNT. Scale bar, 200 nm. c) Element mapping images of BRPH@MWCNT using energy-dispersive X-ray spectroscopy (EDS). Scale bar, 50 nm. d) Probing the formation of BRPH using high-resolution TEM. Scale bar, 5 nm. The red dotted boxes separate the crystalline BP (inside) and amorphous RP (outside). The inset shows the fast Fourier transformed (FFT) patterns of RP and BP. e) XRD patterns of BRPH@MWCNT and RP@MWCNT. f) Raman spectra of MWCNT, RP and BRPH@MWCNT. g) Density of states (DOS) show the difference of bandgap distribution manner for BP and RP individuals. h) Differential charge density and built-in electric field at the BP/RP heterojunction interface, the yellow and cyan electron clouds respectively show the electron accumulation and depletion.

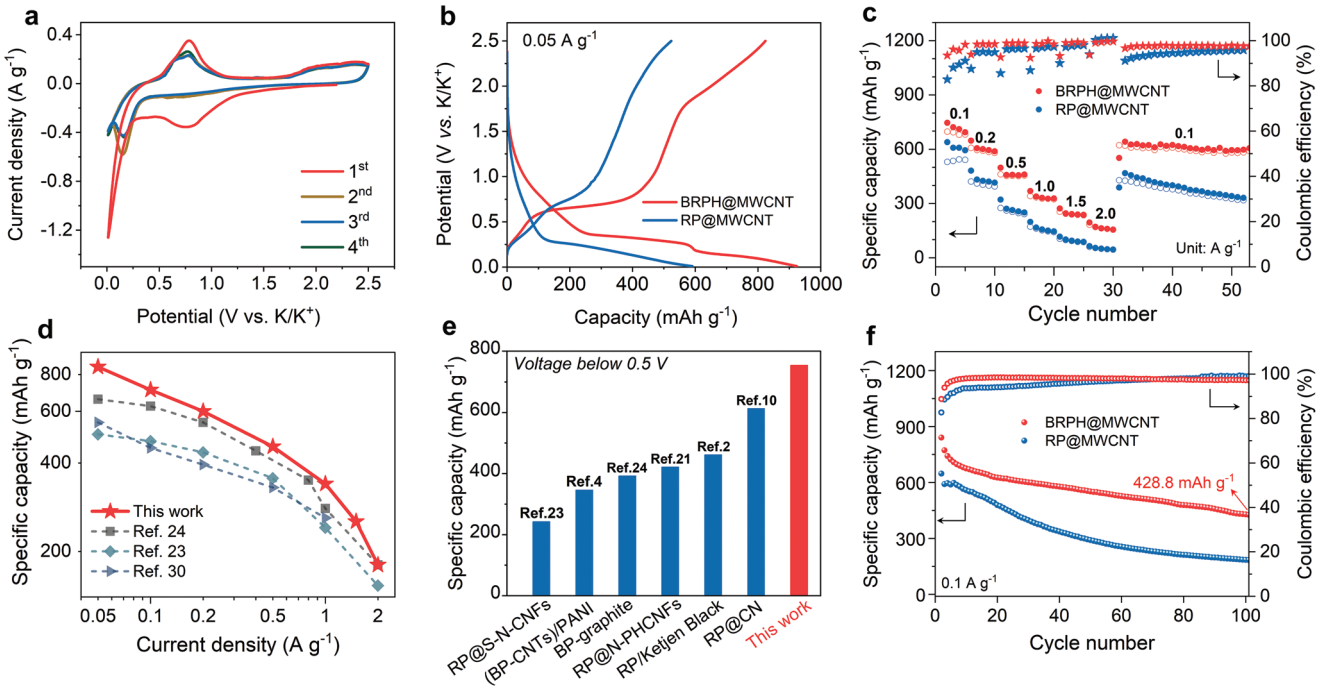

Figure 2. Electrochemical performances of the BRPH@MWCNT. a) CV curves of BRPH@MWCNT (with BP/RP ratio of 0.9) during the first four cycles. Scan rate, 0.1 mV s^{-1}. b) Galvanostatic discharge–charge curves of RP@MWCNT and BRPH@MWCNT at a current density of 0.05 A g^{-1}. c) Comparison of the rate performance of RP@MWCNT and BRPH@MWCNT at different current densities. d) Comparison of the rate performance of BRPH@MWCNT with state-of-the-art elemental P-based anode materials.[23,24,30] e) Comparison of the specific capacity of this work with state-of-the-art phosphorus-based materials at 0.1 A g^{-1} in the voltage range of 0.01 to 0.5 V versus K/K^+.[2,4,10,21,23,24] f) Cycling performance of RP@MWCNT and BRPH@MWCNT at the current density of 0.1 A g^{-1}. All the BRPH@MWCNT sample was subjected to a BP/RP ratio of 0.9 unless otherwise specified.

capacity of 923 mAh g^{-1} at 0.05 A g^{-1}, compared with only 600 mAh g^{-1} of RP@MWCNT (Figure 2b). In addition, a much lower overpotential (≈0.25 V) was demonstrated in BRPH@MWCNT compared with ≈0.5 V of RP@MWCNT (Figure 2b), suggesting the promoted charge transfer owing to the BP/RP heterostructure. We also verified the negligible capacities derived from MWCNT in BRPH@MWCNT (Figure S8, Supporting Information).

The presence of abundant BP/RP heterostructures afforded excellent rate capability at increasing current densities from 0.1 to 2.0 A g^{-1} (Figure 2c). For instance, the specific capacity of BRPH@MWCNT (BP/RP ratio of 0.9) reached 335 mAh g^{-1} at 1 A g^{-1}, which was far beyond the capacity of BP@MWCNT (168.5 mAh g^{-1}, Figure S5b, Supporting Information) and RP@MWCNT (174.4 mAh g^{-1}, Figure 2c). At 2 A g^{-1}, the BRPH@MWCNT delivered a decent specific capacity of 194.6 mAh g^{-1} compared with only 64.2 mAh g^{-1} for RP@MWCNT counterpart. In addition, the BP/RP heterostructure could retain 92.5% of the original capacity after the rate test, compared with only 65.3% of RP@MWCNT, suggesting the robust heterostructure integrity during repeated K-ion alloying reaction. Remarkably, our BRPH@MWCNT showed excellent rate performances compared with state-of-the-art counterparts (Figure 2d).[23,24,30,31] Our BRPH@MWCNT delivered the highest reversible discharge capacity below 0.5 V compared with state-of-the-art elemental P anodes of PIBs (Figure 2e),[2,4,10,21,23,24,30–35] which represented an important practial parameter that affected the charging process of full cells.

The cycling performances of BRPH@MWCNT and RP@MWCNT were further investigated based on different current densities. At a low current density of 0.1 A g^{-1}, a reversible specific capacity of 428.8 mAh g^{-1} was achieved after 100 cycles for BRPH@MWCNT, compared with only 184.0 mAh g^{-1} of RP@MWCNT after 100 cycles (Figure 2f). In stark contrast, a rapid capacity decay was demonstrated for RP@MWCNT, which only retained 19.6% of the original capacity after 100 cycles. At a higher current density of 0.8 A g^{-1}, the BRPH@MWCNT showed a capacity increase at first, originated from the continuous activation of the inner active species in BRPH@MWCNT,[36,37] and could retain 83.3% of the original capacity after 300 cycles (Figure S9, Supporting Information). This suggests that the BP/RP heterostructure significantly improves the reversibility of the K-P alloying/dealloying process.

The BP/RP heterostructure showed facilitated reaction kinetics. We performed electrochemical impedance spectroscopy (EIS) to investigate the variation of charge transfer resistance (R_{ct}) during continuous potassiation. RP@MWCNT exhibited large R_{ct}, for example, 1410 Ω (2.5 V) and 7458 Ω (0.01 V) (**Figure 3**a,b; Table S2, Supporting Information), which indicated the inferior K-ion transfer during potassiation (Figure S10, Supporting Information). In comparison, BRPH@MWCNT showed much lower R_{ct}, for example, 600 Ω (2.5 V) and 981 Ω (0.01 V), suggesting the efficient K-ion transfer that facilitated deep potassiation process. Galvanostatic intermittent titration (GITT) revealed much higher K-ion diffusion coefficients (D_{K+}) of BRPH@MWCNT than that of RP@MWCNT

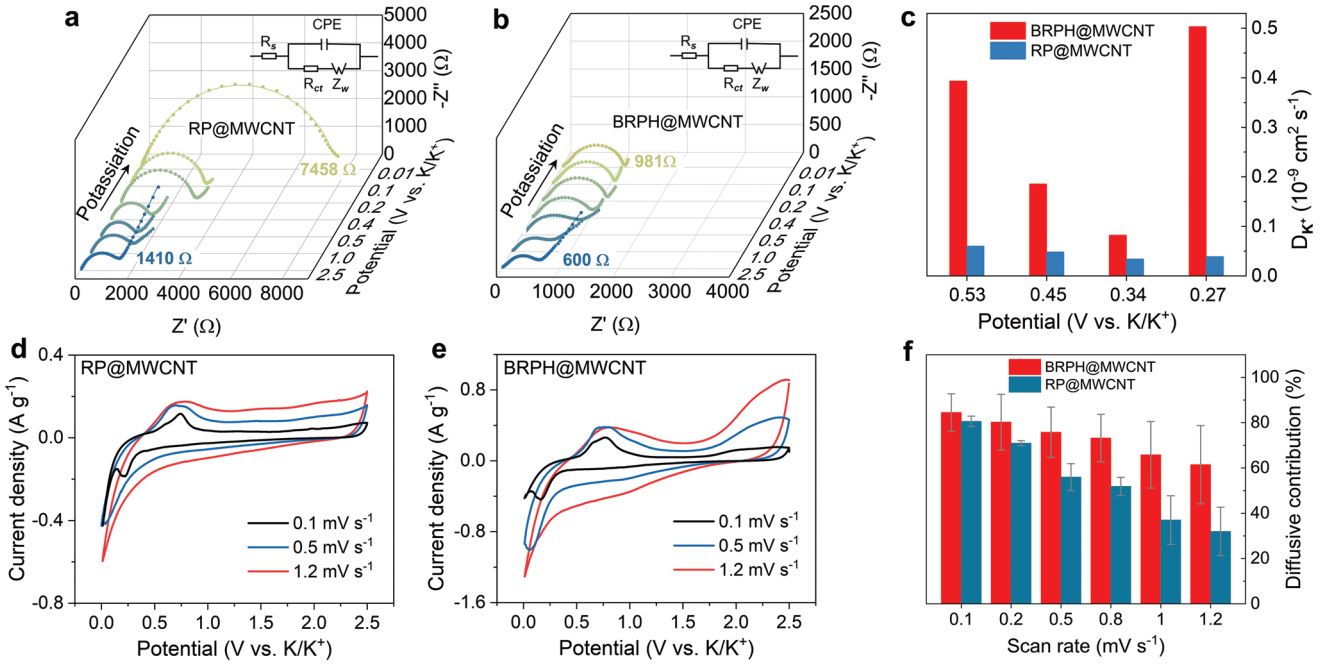

Figure 3. Potassiation kinetics analysis. a,b) EIS analysis of the steady potassiation from 2.5 to 0.01 V based on RP@MWCNT and BRPH@MWCNT. Both anodes were cycled after 20 cycles at 0.1 A g^{-1}. The insets show the equivalent circuits for fittings, where R_s and R_{ct} represent the solution resistance and charge transfer resistance, respectively. CPE and Z_w are the constant phase element and Warburg element, respectively. c) Comparison on K-ion diffusion coefficients (D_{K+}) of RP@MWCNT and BRPH@MWCNT derived from GITT measurement. d,e) CV curves of RP@MWCNT and BRPH@MWCNT at a variety of scan rates, respectively. f) Comparison on diffusive capacity contribution of BRPH@MWCNT and RP@MWCNT calculated from two parallel CV results in Figure S12, Supporting Information.

at the representative potassiation plateau (0.53–0.27 V), indicating the facilitated K-ion diffusion originated from the heterostructure (Figure 3c and Figure S11, Supporting Information). Kinetic studies revealed that both BRPH@MWCNT and RP@MWCNT showed a diffusion-dominant contribution (higher than 70%) at low scan rates of 0.1 and 0.2 mV s^{-1}. At higher scan rates (e.g., 1.2 mV s^{-1}), the BRPH@MWCNT anode well maintained the diffusion contribution of more than 60% (Figure 3f). In stark contrast, the diffusion contribution of RP@MWCNT rapidly decreased to less than 32% (Figure 3d–f and Figure S12, Supporting Information). These confirmed the effective regulation on K-ion immigration through abundant heterojunctions between BP and RP.

Unveiling the working mechanism of BP/RP heterostructure has important implication for further improvement on battery performance. The potassiation process of the heterostructure was revealed by first-principles calculations based on density functional theory (DFT) (see details in Supporting Information). Two stabilized K-ion adsorption sites at BP/RP heterostructure interface (named K_{1H} and K_{2H}) and bare RP interface (named K_{1R} and K_{2R}) were demonstrated in **Figure 4**a–d. BRPH showed more negative adsorption energy (–0.83 eV) than that of RP (–0.36 eV) (Figure 4g), suggesting enhanced K-ion adsorption at the heterostructure interface.[38] Simulations of the K-ion diffusion pathway showed a significantly reduced energy barrier of 0.61 eV for BP/RP heterostructure compared with 1.51 eV for RP (Figure 4e,f,h). These suggested the facilitated reaction kinetics attributed to the heterostructure, in accordance with the remarkable rate capability of BRPH@MWCNT (Figure 2c).[39]

We further performed *Operando* XRD to probe the evolution of potassiation/depotassiation products during battery cycling (Figure 4i). During the initial potassiation process from 2.4 to 1.0 V, a diffraction peak at 29.7° emerged, which corresponded to the (130) plane of K_4P_3 (JCPDS No. 79–0033). Further potassiation from 1.0 to 0.20 V strengthened the K_4P_3 peak, accompanied by a new Bragg peak at 18.2° corresponding to the (100) plane of K_3P (JCPDS No. 74–0128). During the final potassiation process from 0.20 to 0.01 V, the peak intensity of K_4P_3 weakened, and the peak of K_3P became dominated (Figure 4i), indicating the formation of K_3P as the final potassiation product. During depotassiation, the peak intensities of K_3P and K_4P_3 went through a reverse process, suggesting the good reversibility of the potassiation/depotassiation procedure. The formation of K_3P was further verified by ex situ XRD and HRTEM (Figures S13 and S14, Supporting Information). These indicated the deep potassiation process with the formation of K_3P as the final potassiation product, attributed to the efficient BP/RP heterostructure that regulated K-ion adsorption and diffusion kinetics, thus promoting the sluggish and capacitive-dominated K-ion storage for elemental P anodes.[2,4,23]

The formation of K_3P was further confirmed by time-of-flight secondary ion mass spectroscopy (TOF-SIMS). Depth profile of K_xP secondary ion fragments showed the normalized ion intensities in the order of $K_4P^+ > K_4P_3^+ > K_3P^+ > KP^+$ (Figure S15, Supporting Information), indicating that K_3P (source of K_4P^+ and K_3P^+ fragments) was one of the main potassiation products of the BRPH@MWCNT anode. In stark contrast, the fully potassiated RP@MWCNT showed the dominant signals of $K_2P_5^+$,

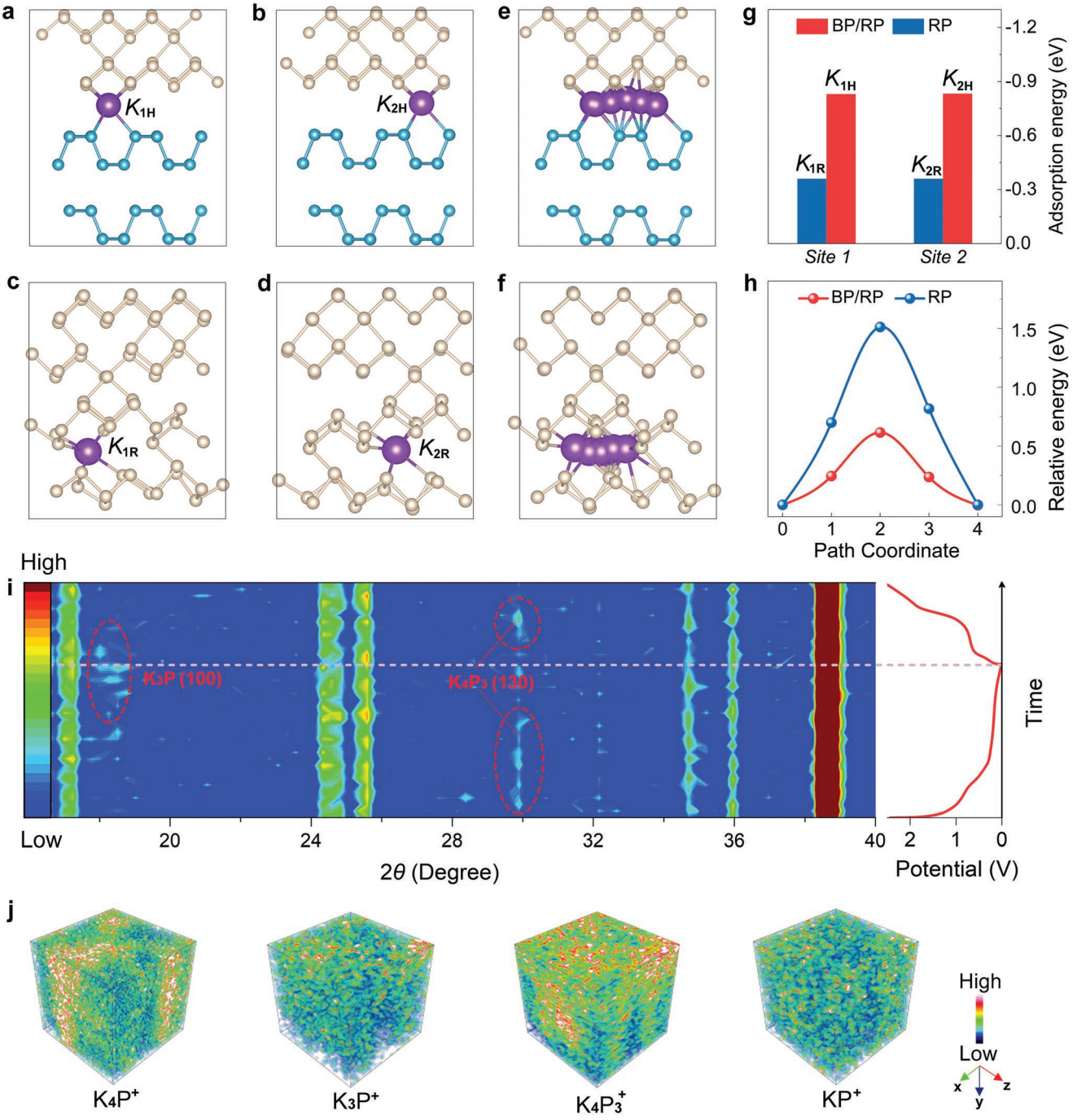

Figure 4. Fast and deep potassiation based on BP/RP heterostructure. a,b) Two K-ion adsorption modes at the BP/RP heterointerface, denoted as K_{1H} and K_{2H}. c,d) Two K-ion adsorption modes in the interlamination of RP, denoted as K_{1R} and K_{2R}. The brown, blue and purple atom balls respectively represent RP, BP and potassium atoms. e,f) K-ion immigration paths in BP/RP heterostructure and RP interlamination, respectively. g) Comparison of the adsorption energy of BP/RP heterostructure and bare RP. h) Dependence of relative energy on the K-ion immigration paths of BP/RP heterostructure and RP interlamination. i) *Operando* XRD patterns of BRPH@MWCNT during the initial discharge/charge process. j) Three-dimensional distributions of K_4P^+, K_3P^+, K_4P^{3+} and KP^+ in a fully discharged BRPH@MWCNT sample using TOF-SIMS depth scan. The analysis area is 100 × 100 μm^2.

$K_2P_2^+$, and $K_5P_4^+$ without K_4P^+ or K_3P^+ fragments (Figures S16 and S17, Supporting Information), which confirmed the failure of deep potassiation process for RP@MWCNT without the efficient heterostructure, and was in accordance with the electrochemical performances. The distribution of the main fragments was also verified by 3D depth profile of TOF-SIMS, suggesting their relatively uniform distribution (Figure 4j). Robust SEI is critical for highly reversible K redox.[40] To better understand the mechanism of the improved cycling stability, we probed the surface composition of cycled BRPH@MWCNT and

RP@MWCNT using XPS. High-resolution F 1s spectra of cycled BRPH@MWCNT showed two pronounced KF peaks at 683.6 and 682.0 eV (Figure S18, Supporting Information),[41,42] while the cycled RP@MWCNT exhibited much weaker KF intensities. The KF-rich SEI might be originated from the facilitated decomposition of FSI^- and $TFSI^-$ induced by the strong built-in electric field at the heterointerface of BP and RP atoms. These indicated the effective regulation on SEI chemistry through the construction of abundant BP/RP heterostructure, which suppressed the parasitic reactions and enhanced the electrochemical reversibility.[43]

The employment of elemental P anode in K-ion full cell represents a critical step for practical application of PIBs, which remains a grand challenge owing to the sluggish reaction kinetics and poor electrochemical reversibility. We produced BRPH@MWCNT/Prussian full cells with a decent negative-to-positive (N/P) ratio of 1.4:1 (**Figure 5**a). The synthesized Prussian blue cathode exhibited a rhombohedral structure with $R\bar{3}m$ space group in XRD (Figure S19, Supporting Information),[44,45] and showed two characteristic discharge plateaus at 4.0 and 3.9 V with high rate capability (Figure S20, Supporting Information). Our BRPH@MWCNT/Prussian full cell showed a specific capacity of 76 mAh g^{-1} at 100 mA g^{-1} based on the total mass of active materials on cathode and anode (Figure 5b,c). The facilitated reaction kinetics of the BRPH@MWCNT anode ensured a good rate performance of the full cell, delivering high current densities up to 300 mA g^{-1} (2.5 C, Figure 5c; Figure S21, Supporting Information). Ragone plot showed the maximal energy and power densities of ≈250 Wh kg^{-1} and ≈1400 W kg^{-1}, respectively, which were highly competitive compared with state-of-the-art K-ion full cells using elemental P anodes (Figure 5d).[24,37] In addition, it could retain 63% of the initial capacity after 100 cycles at 300 mA g^{-1} (Figure 5e), suggesting the high electrochemical reversibility of both electrodes. As a comparison, we conducted a RP@MWCNT/Prussian blue full cell and observed a sharp capacity decrease during the initial 40 cycles with an optimized N/P ratio of 1.3 (Figure S22, Supporting Information). Moreover, even at a much lower N/P ratio of 1.1, the BRPH@MWCNT/Prussian full cell could retain 46% of the original capacity after 100 cycles at 200 mA g^{-1} (Figure S23, Supporting Information). As a proof-of-concept, a BRPH@MWCNT/Prussian blue pouch cell could be used to charge a mobile phone (Figure 5f).

3. Conclusion

In conclusion, we show that rational heterostructure engineering can be an effective approach for unlocking deep and fast K-ion storage in elemental P anode, which enables the formation of K_3P as the deep potassiation product. Mechanism analysis indicates the abundant heterostructure interfaces significantly promote K-ion adsorption, injection and immigration, thus facilitating the reaction kinetics of K-ion storage. Of all the reported PIB anodes based on elemental P, our BRPH@MWCNT anode demonstrates a highly reversible specific capacity of 923 mAh g^{-1} at 0.05 A g^{-1}, high rate capability at 2 A g^{-1}, and excellent cycling performance of 300 cycles.

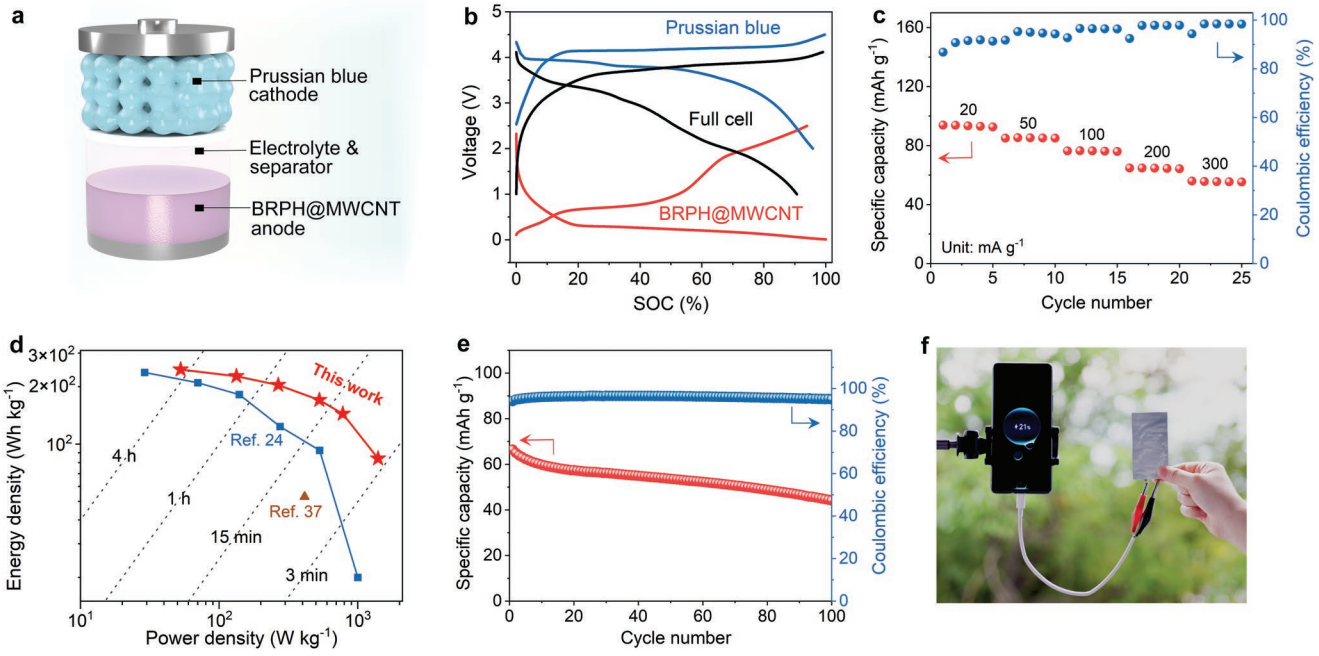

Figure 5. High-performing BRPH@MWCNT/Prussian blue full cells. a) Schematic illustration of the BRPH@MWCNT/Prussian blue full cell. b) Charge/discharge profiles of the K metal/BRPH@MWCNT half cell (red curve), K metal/Prussian blue half cell (blue curve) and BRPH@MWCNT/Prussian blue full cell (yellow curve) at the current density of 100 mA g^{-1}. c) Rate performance of the BRPH@MWCNT/Prussian blue full cell with an N/P ratio of 1.4. d) Ragone plot of our BRPH@MWCNT/Prussian blue full cell compared with other PIBs using phosphorus anodes.[24,37] The specific capacity, energy, and power densities were all calculated based on the total mass of active materials on both electrodes. e) Cycling performance of a BRPH@MWCNT/Prussian blue full cell at the current density of 300 mA g^{-1}. f) A BRPH@MWCNT/Prussian blue pouch cell charged a mobile phone.

Remarkably, its excellent electrochemical performance enables the production of practical K-ion full batteries with high energy and power densities. Our results can unlock elemental P-based anodes for practical PIBs, and inspire other sluggish and irreversible battery chemistries toward low-cost and large-scale energy storage.

4. Experimental Section

Synthesis of BRPH@MWCNT and RP@MWCNT: The BRPH@MWCNT was prepared via a facile solvent-thermal method.[15] MWCNT (diameter of ≈5–15 nm, Xfnano) was pretreated with 1 M KOH (AR, Titan) solution at 60 °C for 5 h to produce –OH group on the surface, denoted as OH-MWCNT. The obtained OH-MWCNT was rinsed using deionized (DI) water for several times and dried at 80 °C. Commercial red phosphorus (97%, Titan) was utilized as the precursor, and the ethane diamine (AR, Sinopharm) solution was employed as a phosphorous chain attacker and structural reconstruction agent. Typically, red phosphorus was hydrothermally pretreated in a stainless-steel autoclave at 200 °C for 12 h to remove the surface oxide residues and produce loosened RP monolith. 450 mg pretreated RP was added into 30 mL ethane diamine solution and stirred under 500 rpm for 30 min, followed by addition of 60 mg OH-MWCNT and a gentle stirring for 30 min. The obtained suspension was solvothermal-treated at 160 °C for 24 h for RP crystallization/phase transition to BP under a high pressure. After cooling down to room temperature, the black precipitate at the bottom was collected and rinsed with DI water for several times using centrifugation until the decantate became nearly neutral. The precipitate was then freeze-dried to obtain the BRPH@MWCNT product. RP@MWCNT was synthesized via a similar approach. To avoid the formation of BP, the RP-ethane diamine solution was acidly treated for precipitation of nanosized RP on OH-MWCNT without solvothermal treatment.[18] Briefly, 450 mg pretreated RP was dissolved into a 30 mL ethane diamine solution under stirring. 60 mg OH–MWCNT was dispersed in 100 mL diluted nitric acid (0.05 M, Sinopharm) and 5 mL ethanol (AR, Sinopharm). The OH–MWCNT suspension was ultrasonicated for 10 min, and dropwise added into the RP-ethane diamine solution under continuous stirring. After that, the RP@MWCNT product was collected and rinsed following the same procedure of BRPH@MWCNT.

Preparation of Electrodes and Electrolyte: Ketjen black (KJ, Shenzhen Kejing Star) and sodium alginate (SA, AR grade, Aldrich) were served as the conductive agent and binder, respectively. Cu and Al foils were used as the current collectors of anode and cathode, respectively. Typically, BRPH@MWCNT (70 wt%), KJ (15 wt%), and SA (15 wt%) were ground using an agate mortar, and dispersed in DI water to form a slurry. The slurry was casted on a precleaned Cu foil using a scraper and dried at room temperature for 5 h. The obtained tape was chopped into circular foils with a diameter of 12 mm with the mass loading of ≈1 mg cm^{-2}. The Prussian blue cathode material was synthesized according to previous literatures.[45,46] The cathode mass loadings were 3.7–4.8 mg cm^{-2}. As for electrolyte fabrication, 4 M potassium bis(fluorosulfonyl) imide (KFSI, battery grade, DodoChem) and 1 M potassium bis(trifluorosulfonyl)imide (KTFSI, battery grade, DodoChem) in the mixture of ethylene carbonate (EC, anhydrous, Titan) and dimethyl carbonate (DMC, Adamas, 99%) solution with volume ratio of 1:1 was prepared as the electrolyte. The salts of KFSI and KTFSI were dried at 120 °C in a vacuum oven before use, and the electrolyte was used after molecular-sieve drying treatment.

Electrochemical Measurements: The electrochemical measurements were conducted in CR2032 coin cells. All the cells were assembled in argon-filled glove box with O_2 < 1 ppm and H_2O < 0.5 ppm. K metal (Sigma Aldrich) was first washed by anhydrous DMC for removal of the bathing oil, and scraped the surface oxide layers using a clean blade before pressed into a thin foil. One layer of GF/D membrane (Whatman) was used as the separator. All cells were aged for 6 h and tested on a Neware battery testing system. The full cells were fabricated in a coin cell or an aluminum laminated pouch at glove box following the typical procedure in the previous work.[44] Before the assembly of full-cell tests, the BRPH@MWCNT anode was pre-potassiated with a K metal separately and discharge to ≈0.1 V for stable SEI formation. Typically for pouch cell fabrication, the Prussian blue cathode foil and BRPH@MWCNT anode foil was pasted on the aluminum laminated pouch using carbon taps (Ted Pella). Two nickel tabs and a GF/A membrane (Whatman) were used as current collector and separator, respectively. Approximately 400 µL electrolyte was involved for each pouch. After heat-sealing, the full-cell pouch was used for powering a cell phone. Galvanostatic charge/discharge profiles of the full cells paired with Prussian blue were conducted in the voltage window from 1 to 4.12 V. The current density and capacity were calculated based on the total mass of active materials on both cathode and anode. The *N*/*P* ratio was calculated based on an BRPH@MWCNT anode capacity of 800 mAh g^{-1} and a Prussian blue cathode capacity of 120 mAh g^{-1}. 1 C for full cell was set to be 120 mA g^{-1} based on total active materials. EIS analyses were conducted on CHI660E electrochemical workstation with the frequency range of ≈0.01 Hz–100 kHz.

Characterizations: XRD was performed on a Rigaku Ultima IV powder X-ray diffractometer via a Cu Kα radiation. SEM and EDS mapping were examined using a ZEISS Gemini 300 SEM with an operation voltage of 5 and 20 kV, respectively. TEM and HRTEM was acquired on a JEOL JEM 2100F transmission electron microscope at 200 kV. TOF-SIMS was conducted on a TOF-SIMS 5–100 instrument made by ION-TOF GmbH, Germany. Positive-ion mode was used for TOF-SIMS tests with analysis chamber pressure below 1.1×10^{-9} mbar, the analysis area was 100×100 μm^2. XPS fine-structure spectra were recorded on a Thermo Fisher Nexsa XPS Microprobe operating at 25 mA and 15 kV. All the binding energies were calibrated to the C 1s peak of 284.8 eV or Cu 2p peak of 930.6 eV. Raman spectra were recorded on a Renishaw inVia confocal Raman microscope with 532 nm excitation laser. TGA was performed on a TGA5500 instrument under N_2 atmosphere from 50 to 800 °C. Nitrogen adsorption/desorption isotherms were collected on an Autosorb-IQ3 analyzer at 77 K. The specific surface areas were calculated using the Brunauer–Emmett–Teller (BET) method in the relative pressure region of 0 to 1.0.

Supporting Information

Supporting Information is available from the Wiley Online Library or from the author.

Acknowledgements

X.Z. and S.G. contributed equally to this work. This work was supported by National Natural Science Foundation of China (22209108), the Key Research and Development Program of Jiangsu Provincial Department of Science and Technology of China (BE2020684), and Jiangsu Carbon Peak Carbon Neutralization Science and Technology Innovation Special Fund (BE2022605).

Conflict of Interest

The authors declare no conflict of interest.

Data Availability Statement

The data that support the findings of this study are available in the supplementary material of this article.

Keywords

altered heterostructures, deep potassiation, interface engineering, phosphorus anodes, potassium-ion batteries

Received: April 1, 2023
Revised: April 19, 2023
Published online: May 1, 2023

[1] W. Zhang, Y. Liu, Z. Guo, *Sci. Adv.* **2019**, *5*, eaav7412.
[2] W. Xiao, X. Li, B. Cao, G. Huang, C. Xie, J. Qin, H. Yang, J. Wang, X. Sun, *Nano Energy* **2021**, *83*, 105772.
[3] S. Zhang, Y. Zhang, Z. Zhang, H. Wang, Y. Cao, B. Zhang, X. Liu, C. Mao, X. Han, H. Gong, Z. Yang, J. Sun, *Adv. Energy Mater.* **2022**, *12*, 2103888.
[4] J. Guan, A. M. Rao, J. Zhou, X. Yu, B. Lu, *Adv. Funct. Mater.* **2022**, *32*, 2203522.
[5] Y. Wu, J. Cheng, Z. Liang, Y. Tang, T. Qiu, S. Gao, R. Zhong, R. Zou, *Small* **2022**, *18*, 2105767.
[6] W. Zhang, J. Mao, S. Li, Z. Chen, Z. Guo, *J. Am. Chem. Soc.* **2017**, *139*, 3316.
[7] S. Zhao, K. Yan, J. Liang, Q. Yuan, J. Zhang, B. Sun, P. Munroe, G. Wang, *Adv. Funct. Mater.* **2021**, *31*, 2102060.
[8] J. Lang, J. Li, X. Ou, F. Zhang, K. Shin, Y. Tang, *ACS Appl. Mater. Interfaces* **2020**, *12*, 2424.
[9] X. Huang, X. Sui, W. Ji, Y. Wang, D. Qu, J. Chen, *J. Mater. Chem. A* **2020**, *8*, 7641.
[10] P. Xiong, P. Bai, S. Tu, M. Cheng, J. Zhang, J. Sun, Y. Xu, *Small* **2018**, *14*, 1802140.
[11] H. Jin, H. Wang, Z. Qi, D. Bin, T. Zhang, Y. Wan, J. Chen, C. Chuang, Y. Lu, T. Chan, H. Ju, A. Cao, W. Yan, X. Wu, H. Ji, L. Wan, *Angew. Chem., Int. Ed.* **2020**, *59*, 2318.
[12] H. Chen, L. Meng, H. Yue, C. Peng, Q. Zhang, G. Zhong, D. Chen, *J Energy Chem* **2022**, *79*, 45.
[13] C. He, J. H. Zhang, W. X. Zhang, T. T. Li, *J. Phys. Chem.* **2019**, *123*, 5157.
[14] Y. Wu, H. B. Huang, Y. Feng, Z. S. Wu, Y. Yu, *Adv. Mater.* **2019**, *31*, 1901414.
[15] F. Liu, R. Shi, Z. Wang, Y. Weng, C. M. Che, Y. Chen, *Angew. Chem., Int. Ed.* **2019**, *58*, 11791.
[16] X. Ma, C. Ji, X. Li, Y. Liu, X. Xiong, *Mater. Today* **2022**, *59*, 36.
[17] D. Zhao, L. Zhang, C. Fu, J. Huang, H. Huang, Z. Li, J. Zhang, C. Niu, *Carbon* **2018**, *139*, 1057.
[18] W. Liu, S. Ju, X. Yu, *ACS Nano* **2020**, *14*, 974.
[19] D. J. Olego, J. A. Baumann, M. A. Kuck, R. Schachter, C. G. Michel, *Solid State Commun.* **1984**, *52*, 311.
[20] Y. Zhang, X. Rui, Y. Tang, Y. Liu, J. Wei, S. Chen, W. R. Leow, W. Li, Y. Liu, J. Deng, B. Ma, Q. Yan, X. Chen, *Adv. Energy Mater.* **2016**, *6*, 1502409.
[21] Y. Wu, S. Hu, R. Xu, J. Wang, Z. Peng, Q. Zhang, Y. Yu, *Nano Lett.* **2019**, *19*, 1351.
[22] X. Lu, W. Lin, Y. Huang, J. Zhang, L. Guan, X. Huang, K. Du, X. Wu, *ACS Appl. Energy Mater.* **2021**, *4*, 9682.
[23] W. Feng, H. Wang, Y. Jiang, H. Zhang, W. Luo, W. Chen, C. Shen, C. Wang, J. Wu, L. Mai, *Adv. Energy Mater.* **2022**, *12*, 2103343.
[24] X. Du, B. Zhang, *ACS Nano* **2021**, *15*, 16851.
[25] S. Zhang, H. J. Qian, Z. Liu, H. Ju, Z. Y. Lu, H. Zhang, L. Chi, S. Cui, *Angew. Chem., Int. Ed.* **2019**, *58*, 1659.
[26] J. Sun, H. W. Lee, M. Pasta, H. Yuan, G. Zheng, Y. Sun, Y. Li, Y. Cui, *Nat. Nanotechnol.* **2015**, *10*, 980.
[27] Y. Zhang, S. Wei, Z. Zhao, X. Pei, W. Zhao, J. Wang, X. Du, D. Li, *Small* **2022**, *18*, 2107258.
[28] T. T. Zhuang, Y. Liu, M. Sun, S. L. Jiang, M. W. Zhang, X. C. Wang, Q. Zhang, J. Jiang, S. H. Yu, *Angew. Chem., Int. Ed.* **2015**, *54*, 11495.
[29] W. Liu, L. Du, S. Ju, X. Cheng, Q. Wu, Z. Hu, X. Yu, *ACS Nano* **2021**, *15*, 5679.
[30] D. Peng, Y. Chen, H. Ma, L. Zhang, Y. Hu, X. Chen, Y. Cui, Y. Shi, Q. Zhuang, Z. Ju, *ACS Appl. Mater. Interfaces* **2020**, *12*, 37275.
[31] W. Zhang, W. K. Pang, V. Sencadas, Z. Guo, *Joule* **2018**, *2*, 1534.
[32] F. Yang, J. Hao, J. Long, S. Liu, T. Zheng, W. Lie, J. Chen, Z. Guo, *Adv. Energy Mater.* **2020**, *11*, 2003346.
[33] D. Su, J. Dai, M. Yang, J. Wen, J. Yang, W. Liu, H. Hu, L. Liu, Y. Feng, *Nanoscale* **2021**, *13*, 6635.
[34] J. Gong, G. Zhao, J. Feng, Y. An, T. Li, L. Zhang, B. Li, Z. Qian, *ACS Nano* **2020**, *14*, 14057.
[35] W. Qiu, H. Xiao, Y. Li, X. Lu, Y. Tong, *Small* **2019**, *15*, e1901285.
[36] H. Yin, W. Shen, H. Qu, C. Li, M. Zhu, *Nano Energy* **2020**, *70*, 104468.
[37] W. Chang, J. Wu, K. Chen, H. Tuan, *Adv. Sci.* **2019**, *6*, 1801354.
[38] S. Geng, T. Zhou, M. Jia, X. Shen, P. Gao, S. Tian, P. Zhou, B. Liu, J. Zhou, S. Zhuo, F. Li, *Energy Environ. Sci.* **2021**, *14*, 3184.
[39] W. Yang, Y. Lu, C. Zhao, H. Liu, *Electron. Mater. Lett.* **2019**, *16*, 89.
[40] M. Zhou, P. Bai, X. Ji, J. Yang, C. Wang, Y. Xu, *Adv. Mater.* **2021**, *33*, 2003741.
[41] J. Li, Y. Hu, H. Xie, J. Peng, L. Fan, J. Zhou, B. Lu, *Angew. Chem., Int. Ed.* **2022**, *61*, e202208291.
[42] N. Xiao, W. D. McCulloch, Y. Wu, *J. Am. Chem. Soc.* **2017**, *139*, 9475.
[43] H. Wang, D. Yu, X. Wang, Z. Niu, M. Chen, L. Cheng, W. Zhou, L. Guo, *Angew. Chem., Int. Ed.* **2019**, *58*, 16451.
[44] H. Sun, P. Liang, G. Zhu, W. H. Hung, Y. Y. Li, H. C. Tai, C. L. Huang, J. Li, Y. Meng, M. Angell, C. A. Wang, H. Dai, *Proc. Natl. Acad. Sci. U. S. A.* **2020**, *117*, 27847.
[45] L. Wang, Y. Lu, J. Liu, M. Xu, J. Cheng, D. Zhang, J. B. Goodenough, *Angew. Chem., Int. Ed.* **2013**, *52*, 1964.
[46] X. Jiang, H. Liu, J. Song, C. Yin, H. Xu, *J. Mater. Chem. A* **2016**, *4*, 16205.